PCCP

ROYAL SOCIETY OF CHEMISTRY

PAPER

View Article Online
View Journal | View Issue

Cite this: *Phys. Chem. Chem. Phys.*, 2021, **23**, 8854

Exchange-biased quantum tunnelling of magnetization in a $[Mn_3]_2$ dimer of single-molecule magnets with rare ferromagnetic inter-Mn_3 coupling†

Tuhin Ghosh,[a] Jonathan Marbey,[b] Wolfgang Wernsdorfer,[cd] Stephen Hill,[b] Khalil A. Abboud[a] and George Christou *[a]

A covalently-linked dimer of two single-molecule magnets (SMMs), $[Mn_6O(O_2CMe)_6(1,3\text{-ppmd})_3](ClO_4)_2$, has been synthesized from the reaction of $[Mn_3O(O_2CMe)_6(py)_3](ClO_4)$ with 1,3-phenylene-*bis*(pyridin-2-ylmethanone) dioxime (1,3-ppmdH_2). It contains two $[Mn^{III}{}_3O]^{+7}$ triangular units linked by three 1,3-ppmd^{2-} groups into an $[Mn_3]_2$ dimer with D_3 symmetry. Solid-state dc and ac magnetic susceptibility measurements showed that each Mn_3 subunit retains its properties as an SMM with an S = 6 ground state. Magnetization *vs.* dc field sweeps on a single crystal reveal hysteresis loops below 1.3 K exhibiting exchange-biased quantum tunnelling of magnetization (QTM) steps with a bias field of +0.06 T. This is the first example of a dimer of SMMs showing a positive exchange bias of the QTM steps in the hysteresis loops, and it has therefore been subjected to a detailed analysis. Simulation of the loops determines that each Mn_3 unit is exchange-coupled with its neighbour primarily through the 1,3-ppmd^{2-} linkers, confirming a weak ferromagnetic inter-Mn_3 interaction of $J_{12} \approx +6.5$ mK ($\hat{H} = -2J\hat{S}_i\cdot\hat{S}_j$ convention). High-frequency EPR studies of a microcrystalline powder sample enable accurate determination of the zero-field splitting parameters of the uncoupled Mn_3 SMMs, while also confirming the weak exchange interaction between the two SMMs within each $[Mn_3]_2$ dimer. The combined results emphasize the ability of designed covalent linkers to generate inter-SMM coupling of a particular sign and relative magnitude, and thus the ability of such linkers to modulate the quantum physics. As such, this work supports the feasibility of using designed covalent linkers to develop molecular oligomers of SMMs, or other magnetic molecules, as multi-qubit systems and/or other components of new quantum technologies.

Received 22nd December 2020,
Accepted 24th March 2021

DOI: 10.1039/d0cp06611g

rsc.li/pccp

Introduction

Single-molecule magnets (SMMs) are individual molecules that function as single-domain nanoscale magnetic particles below a certain blocking temperature, T_B.[1–5] Among classical applications, they could potentially be used as components in molecular spintronics devices, *i.e.*, electronics based on the spin degree of freedom in addition to the charge,[6,7] and as memory units to each store one bit of classical information as the orientation of their magnetization vector. The latter would lead to ultra-high density 2D information storage for ordered arrays on surfaces and, if the technology were to be developed to read and write information in a truly 3D crystalline lattice by addressing individual molecules in 3D space, then even more orders of magnitude of increase in information storage densities would be achieved. Crystallinity is, in fact, one of the advantages that molecular chemistry brings to nanomagnetism, together with solubility, true monodispersity (in size and shape), structural characterization to atomic resolution by single-crystal X-ray crystallography, a shell of organic ligands that can be modified as desired by standard solution methods, thereby permitting targeted modification of redox potentials and other properties, and the study by various techniques in both solid and solution phases. These molecular advantages of SMMs have also allowed

[a] *Department of Chemistry, University of Florida, Gainesville, Florida, 32611-7200, USA. E-mail: christou@chem.ufl.edu*
[b] *National High Magnetic Field Laboratory and Department of Physics, Florida State University, Tallahassee, Florida 32310, USA*
[c] *Karlsruher Institut für Technologie (KIT), Physikalisches Institut, Wolfgang-Gaede-Str. 1, D-76131 Karlsruhe, Germany*
[d] *Institute of Quantum Materials and Technologies (IQMT), Hermann-von-Helmholtz-Platz 1, Gebäude 640, 76344 Eggenstein-Leopoldshafen, Germany*

† Electronic supplementary information (ESI) available: Crystallographic details in CIF format, bond valence sums, structural figures, magnetic data, EPR data. CCDC 2022761. For ESI and crystallographic data in CIF or other electronic format see DOI: 10.1039/d0cp06611g

discovery of new quantum phenomena within the nanomagnetism arena, such as quantum tunnelling of magnetization (QTM),[8,9] quantum phase interference,[10–12] quantum superposition and entanglement states[13–15] and spin–spin cross relaxation.[16] Such quantum properties consequently led to SMMs also being proposed as components in next-generation technologies such as quantum sensors and quantum memories (qubits) employed in quantum computing applications.[17–20] In contrast, QTM was recognized as detrimental to the prospects of using SMMs for classical information storage, since it would lead to dissipation of the information as the magnetization orientation equilibrated, but one potential solution to this problem was provided when hydrogen-bonded $[Mn_4]_2$ dimers of $[Mn_4O_3Cl_4(O_2CEt)_3(py)_3]$ SMMs with $S = 9/2$ were shown by hysteresis loop studies to shut down the QTM at zero field as the weak antiferromagnetic (**AF**) exchange interaction between each SMM and its neighbour provided an exchange-bias field that shifted the QTM transition away from zero field.[13–15,21] Further, this inter-SMM interaction was also found to generate quantum superposition/entanglement states of the two SMMs, a process relevant to their potential applications to quantum-based technxologies.[13]

In order to provide greater synthetic control of the degree of oligomerization, and the sign of the inter-SMM exchange interaction, we have more recently turned to covalent linkage by dioximate or dicarboxylate groups of the Mn_3 SMM $[Mn_3O(O_2CMe)_3(mpko)_3](ClO_4)$ (**2**; mpkoH = methyl-2-pyridylketone oxime) (Fig. 1) with $S = 6$. Such covalent linkage of SMMs and other magnetic molecules is already being explored extensively, in most cases leading to 1-, 2- and 3D polymeric networks,[22–37] as well as a series of Cr_7Ni wheel dimers by modifying the organic linkers.[38–40] Proof-of-feasibility for our own approach was the reported $[Mn_3]_4$ tetramer linked by non-rigid dioximate groups,[41] and the demonstration of exchange-biased QTM in the hysteresis loops due to weak **AF** coupling through the linker. We then used the directional bonding approach for production of supramolecular assemblies[42] to design a rigid 'V-shaped' dioximate that successfully gave a targeted $[Mn_3]_2$ dimer with three dioximate linkers, parallel Mn_3 planes, and relatively weak ferromagnetic (**F**) inter-Mn_3 coupling, which allowed study of the generated quantum superposition states by high-frequency EPR (HFEPR) in both solid and solution phases for the first time.[43] However, we were foiled by extremely rapid solvent loss in the other major objective of analysing the exchange-biased QTM transitions within a **F** $[Mn_3]_2$ dimer because it prevented magnetization hysteresis studies on a μ-SQUID apparatus.[44]

In order to overcome the latter disappointment, in the present work we have extended our efforts by designing and synthesizing another dioximate linker that we predicted would give a $[Mn_3]_2$ dimer and **F** inter-Mn_3 coupling. Thus, we have chosen to link two oxime groups with a 1,3-phenylene unit to give a 'V-shaped' dioxime 1,3-ppmdH_2 (Fig. 1) that was predicted (i) to yield an $[Mn_3]_2$ dimer rather than a higher oligomer, and (ii) to give **F** inter-Mn_3 coupling since it is known from the organic spin literature that the 1,3-phenylene unit will give **F** coupling between two organic radical groups that it links.[45,46]

We herein report a new covalently-linked $[Mn_3]_2$ dimer that has been successfully synthesized using the new 1,3-ppmdH_2 dioxime and which possesses the targeted **F** inter-Mn_3 coupling and parallel Mn_3 planes. We describe in detail its structure, magnetic properties, analysis of its magnetization hysteresis loops showing QTM steps undergoing a positive exchange bias from the presence of **F** coupling between Mn_3 neighbours, and variable-temperature and -frequency HFEPR spectra that enable precise evaluation of the zero-field splitting (ZFS) parameters of the individual Mn_3 SMMs and an assessment of the intra-dimer exchange coupling strength. This work thus emphasizes the power of molecular chemistry to attain oligomers of SMMs using designed covalent linkers that introduce inter-SMM exchange interactions of a desired type and relative magnitude. It also shows how synthetic chemistry can modulate the quantum properties of magnetic molecules, control crucial to developing new 21st century spin-based technologies.

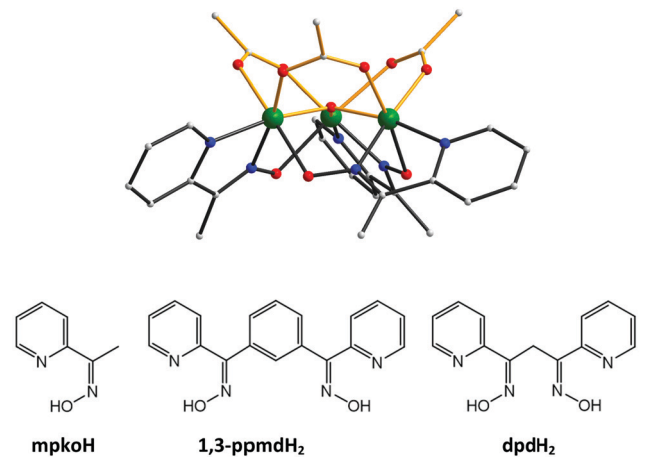

Fig. 1 (top) Structure of the cation of monomer **2** viewed along the Mn_3 plane showing the tripodal arrangement of the three acetate and three $mpko^-$ groups. Colour code: Mn, green; N, blue; O, red; C, gray. (bottom) Structures of mpkoH, 1,3-ppmdH_2 and dpdH_2.

Experimental section

Synthesis

All manipulations were performed under aerobic conditions using chemicals and solvents as received unless otherwise stated. $[Mn_3O(O_2CMe)_6(py)_3](ClO_4)$ (**1**) was prepared according to the literature method.[47] The diketone 1,3-phenylene-*bis*(pyridine-2-ylmethanone) was prepared as previously reported[48] and converted to the dioxime (1,3-ppmdH_2) using hydroxylamine (Fig. S1 of ESI†).[49] CAUTION! Although no such behaviour was encountered, perchlorate salts are potentially explosive and should be used in small quantities with utmost care.

$[Mn_6O_2(O_2CMe)_6(1,3\text{-ppmd})_3](ClO_4)_2$ (3)

A brown solution of complex **1** (0.044 g, 0.050 mmol) in CH_2Cl_2/EtOH (25 : 1 v/v) was treated with solid 1,3-ppmdH_2 (0.024 g, 0.075 mmol) and the solution stirred for 1 hour at room temperature. It was then filtered, and the dark brown filtrate

was maintained undisturbed at ambient temperature. X-ray quality black crystals of **3**·3py·12CH_2Cl_2 slowly formed over 3 days in a 30% yield based on Mn. The crystallographic sample was kept in mother liquor to avoid rapid solvent loss, otherwise the crystals were collected by filtration, washed with Et_2O, and dried by two different methods to assist the magnetism studies. Method A: the crystals were dried under vacuum. Anal. Calcd (found) for **3**·6H_2O ($C_{66}H_{66}Cl_2Mn_6N_{12}O_{34}$): C 40.20 (40.45); H 3.37 (3.05); N 8.52 (8.29). Method B: the crystals were dabbed dry with tissue paper and maintained at ambient temperature and pressure. Anal. Calcd (found) for **3**·3py·H_2O ($C_{81}H_{71}Mn_6N_{15}O_{29}Cl_2$): C 45.91 (45.92); H 3.38 (3.08); N 9.91 (9.83). Selected IR data (cm^{-1}): 1571 (s), 1391 (s), 1460 (s), 1336 (m), 1205 (m), 1118 (s), 1035 (w), 716 (m), 661 (m), 622 (s). Crystals dried by both methods degrade too much to permit X-ray characterization.

X-ray crystallography

X-ray data were collected at 100 K on a Bruker DUO diffractometer using MoK$_\alpha$ radiation (λ = 0.71073 Å) and an APEXII CCD area detector. A suitable crystal of **3**·3py·12CH_2Cl_2 was adhered to a glass fibre with an oil-based cryoprotectant, mounted on a goniometer, and cooled to 100 K for data collection. Raw data frames were read by program SAINT[50] and integrated using 3D profiling algorithms. The resulting data were reduced to produce *hkl* reflections, their intensities and estimated standard deviations. The data were corrected for Lorentz and polarization effects, and numerical absorption corrections were applied based on indexed and measured faces. The structures were solved and refined in SHELXTL2014,[50] using full-matrix least-squares refinement on F^2. The non-H atoms were refined with anisotropic thermal parameters, and all the H atoms were placed in calculated, idealized positions and refined as riding on their parent atoms.

The asymmetric unit consists of a 1/6 Mn_6 cationic cluster lying on a 32 symmetry element, a disordered ClO_4^- anion lying on a C_3 axis, a $\frac{1}{2}$ pyridine molecule located on a C_2 axis, one CH_2Cl_2 molecule in a general position and a second very disordered one. The latter could not be modeled properly, thus program SQUEEZE,[51] a part of the PLATON package of crystallographic software,[52] was used to calculate the solvent disorder area and remove its contribution to the overall intensity data. In the final cycle of refinement, 4576 reflections (of which 3321 were observed with $I > 2\sigma(I)$) were used to refine 252 parameters, giving R_1, wR_2 and S (goodness of fit) of 4.21%, 10.37% and 1.040, respectively. Unit cell data and structure refinement details are listed in Table 1.

Physical and spectroscopic measurements

Infrared spectra were recorded in the solid state as KBr disks on a Nicolet Nexus 670 FTIR spectrometer in the 400–4000 cm^{-1} range. Elemental analyses (C, H, and N) were performed by Atlantic Microlab, Inc. Variable-temperature direct current (dc) and alternating current (ac) magnetic susceptibility data were collected at the University of Florida using a Quantum Design MPMS-XL SQUID magnetometer equipped with a 7 T magnet and operating in the 1.8–300 K range. All the magnetic measurements were carried out on crushed vacuum- or air-dried microcrystalline samples that were embedded in an eicosane matrix to prevent torquing. Pascal's constants were utilized to estimate the diamagnetic correction, and contributions from the eicosane and gel capsule were measured as a blank; all these were subtracted from the experimental susceptibility to give the true molar paramagnetic susceptibility (χ_M).[53] Dc magnetization (M) *vs.* field (H) and temperature (T) data were fit by a matrix diagonalization method using the program MAGNET.[54] Ultra-low-temperature (<1.8 K) dc magnetization hysteresis scans and relaxation *vs.* time measurements were performed at KIT/IQMT using an array of micro-SQUIDS.[44] The high sensitivity of this magnetometer allows the study of single crystals of SMMs of the order of 10–500 μm, and the field can be applied in any direction by separately driving three orthogonal coils. HFEPR powder spectra were collected at the Electron Magnetic Resonance facility of the U.S. National High Magnetic Field Laboratory using a broadband (25 to 600 GHz) transmission probe in which microwaves are propagated into and out of a 17 T superconducting magnet (Oxford Instruments, UK) through cylindrical light pipes.[55] Tunable microwave radiation was generated using a phase-locked solid-state source (Virginia Diodes Inc.) operating at 13 ± 1 GHz, followed by a chain of solid-state multipliers and amplifiers. Field modulation was employed in conjunction with a phase-sensitive homodyne detection scheme using a liquid helium-cooled bolometer as a detector (QMC Instruments, UK), yielding derivative-mode (dI/dH, where I is the absorption intensity) spectra. Temperature control was achieved using a helium gas flow cryostat (Oxford Instruments, UK). Spectral simulations were performed using the program EasySpin.[56]

Table 1 Crystal data and structure refinement parameters for complex **3**

Parameter	**3**·3py·12CH_2Cl_2
Formula[a]	$C_{93}H_{93}Cl_{26}Mn_6N_{15}O_{28}$
FW, g mol^{-1} [a]	3120.16
Crystal system	Trigonal
Space group	$P\bar{3}1c$[b]
a, Å	16.7906(7)
b, Å	16.7906(7)
c, Å	24.3807(10)
V, Å^3	5952.6(6)
Z	2
T, K	100(2)
λ, Å[c]	0.71073
ρ_{calc}, g cm^{-3}	1.741
μ, mm^{-1}	1.279
R_1[de]	0.0421
wR_2[f]	0.1037
GOF on F^2	1.040
$\Delta\rho_{max,min}$/eÅ^{-3}	1.262, −0.718

[a] Including solvent molecules. [b] $\alpha = \beta = 90°$, $\gamma = 120°$. [c] Graphite monochromator. [d] $I > 2\sigma(I)$. [e] $R_1 = \Sigma(||F_o| - |F_c||)/\Sigma|F_o|$. [f] w$R_2 = [\Sigma[w(F_o^2 - F_c^2)^2]/\Sigma[w(F_o^2)^2]]^{1/2}$, $w = 1/[\sigma^2(F_o^2) + (mp)^2 + np]$, where $p = [\max(F_o^2, 0) + 2F_c^2]/3$. m & n are constants.

Results and discussion

Syntheses

The synthetic strategy is based on the previous observation that non-SMM $[Mn_3O(O_2CMe)_6(py)_3](ClO_4)$ (**1**) reacts with three equiv

of the mono-oxime mpkoH (Fig. 1) to yield $[Mn_3O(O_2CMe)_3(mpko)_3](ClO_4)$ (**2**).[57] The cation of **2** (Fig. 1) has virtual C_3 symmetry with the acetate and $mpko^-$ ligands on opposite sides of the Mn_3 plane, and the tripodal arrangement of the three oximates made this SMM an attractive building-block for oligomerization as their replacement with dioximates should give molecular oligomers rather than polymers. In fact, according to the directional bonding approach for production of supramolecular assemblies, the combination of a ~109° ditopic dioximate group and a tritopic Mn_3 unit should give a $[Mn_3]_2$ dimer with three dioximate linkers and parallel Mn_3 planes.[42] Thus, as stated in the introduction, we targeted and successfully prepared 1,3-phenylene-*bis*(pyridin-2-ylmethanone) dioxime (1,3-ppmdH_2) (Fig. 1) in which two 2-pyridyl ketone oxime groups are linked *via* a 1,3-phenylene unit to give a 'V-shaped' (~120°) dioxime. A search of the literature revealed no previous use of 1,3-ppmdH_2 in inorganic chemistry.

The reaction between **1** and 1,3-ppmdH_2 in a 2 : 3 ratio in CH_2Cl_2/EtOH (25 : 1 v/v), the EtOH to improve the dioxime's solubility, led to a darkening of the solution from brown to dark brown and subsequent isolation of black crystals of the targeted $[Mn_3]_2$ dimer $[Mn_6O_2(O_2CMe)_6(1,3\text{-ppmd})_3](ClO_4)_2$ (**3**) as **3**·3py·$12CH_2Cl_2$ in 30% yield (eqn (1)).

$$2[Mn_3O(O_2CMe)_6(py)_3]^+ + 3\ 1,3\text{-ppmd}H_2 \rightarrow [Mn_6O_2(O_2CMe)_6(1,3\text{-ppmd})_3]^{2+} + 6MeCO_2H + 6py \quad (1)$$

Description of structure

Complex **3** is shown in Fig. 2 as a side-view stereopair and a top-view; important metric parameters are collected in Table 2. The Mn_6 cation has virtual and crystallographic D_3 symmetry, the asymmetric unit thus containing only 1/6 of the Mn_6 cluster with all six Mn atoms symmetry equivalent. The Mn_6 cation comprises two $\{Mn^{III}{}_3(\mu_3\text{-}O^{2-})\}^{7+}$ units connected by three 1,3-ppmd^{2-} groups to give a $[Mn_3]_2$ dimer. Each 1,3-ppmd^{2-} oximate unit *N*,*N*-chelates a Mn and bridges with its O atom to a neighbouring Mn. Peripheral ligation is provided by a syn–syn μ-$MeCO_2^-$ bridging each Mn_2 pair. The Mn^{III} oxidation state and the non-protonated nature of the μ_3-O^{2-} were confirmed by bond valence sum (BVS) calculations[58] (Table S1 of ESI†). The Mn Jahn–Teller (JT) elongation axes (green bonds in Fig. 2, top) are tilted 46.48° from being perpendicular to the Mn_3 plane and are aligned in a propeller fashion. Each of the μ_3-O^{2-} ions lies slightly above the Mn_3 plane by (~0.28 Å), and the Mn–N–O–Mn torsion angles are relatively large (ϕ = 14.7°) (Table 2). The two Mn_3 planes are parallel, 8.652 Å apart (centroid···centroid; $O^{2-}\cdots O^{2-}$ = 9.220 Å) and nearly eclipsed (Fig. 2, bottom). Interestingly, the three py solvent molecules are ordered and symmetry related, each π-stacking with two pyridyl rings of 1,3-ppmd^{2-} linkers on neighbouring Mn_3 units giving a three-layer π-stacked column (Fig. S2 of ESI†),[59] whereas the CH_2Cl_2 solvent molecules have minimal contact with the cation of **3**. Drying under vacuum removes both py and CH_2Cl_2 molecules, whereas air-drying at ambient pressure removes only the latter.

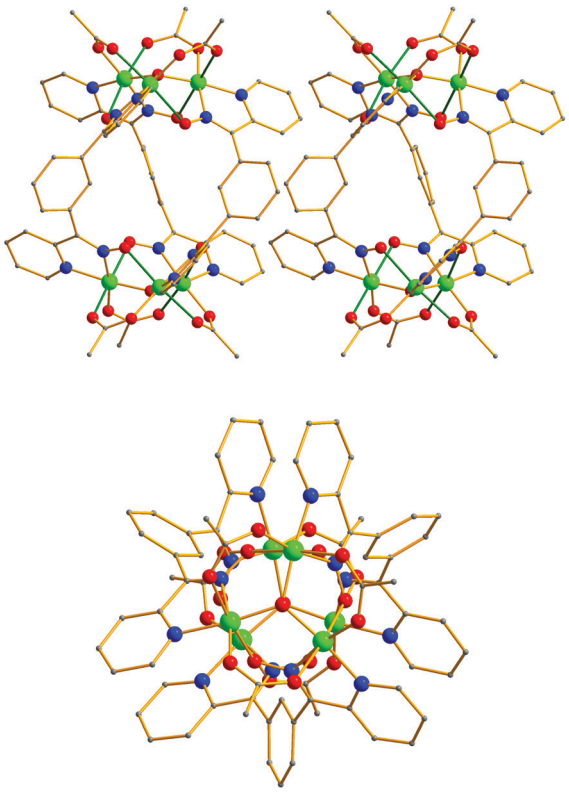

Fig. 2 Complete cation of **3** viewed (top) as a stereopair almost along a C_2 symmetry axis, with the JT axes indicated as green bonds, and (bottom) along the C_3 axis. Colour code: Mn, green; N, blue; O, red; C, grey. Hydrogen atoms have been omitted for clarity.

Table 2 Selected metric parameters (Å, °) for monomer **2**[57] and dimers **3** and **4**[43]

Parameter[a]	**2**[b]	**3**[c]	**4**[c]
Mn_3 triangle	Isosceles	Equilateral	Equilateral
Mn···Mn	3.196[7]	3.198(1)	3.200(1)
Mn1–O^{2-}	1.868[2]	1.868(1)	1.870(1)
Mn1–O(carb)	1.923[5]	1.914(2)	1.935(2)
Mn1–O(carb)	2.200[22]	2.221(2)	2.200(2)
Mn1–N(ox)	2.010[2]	2.011(2)	2.012(2)
Mn1–O(ox)	2.190[17]	2.248(2)	2.167(2)
Mn1–N(py)	2.038[18]	2.019(2)	2.033(2)
Mn–O^{2-}–Mn	117.57[52]	117.73(5)	117.64(5)
O^{2-}-to-Mn_3 plane	0.29	0.28	0.29
Mn–N–O–Mn[d]	11.2	14.7	3.9

[a] carb = carboxylate, ox = oximate, py = pyridyl. [b] Averaged to virtual C_3 symmetry; in [] is the maximum deviation from the mean. [c] Crystallographic D_3 symmetry. [d] Mn–N–O–Mn oxime torsion angle.

Since the three py molecules are intimately associated with the dimer structure, as described above, they likely help maintain a higher symmetry of the dimer in the air-dried crystals than in the vacuum-dried ones (*vide infra*). A packing diagram shows all $[Mn_3]_2$ dimer cations in the crystal to be parallel (Fig. S2 of ESI†).[60] The closest inter-dimer Mn···Mn separation is 8.545 Å.

An important question is whether the linkage into a dimer perturbs the Mn_3 structure, and selected core metric parameters for monomer **2** and dimer **3** are therefore compared in Table 2, which also includes data for previous dimer

$[(Mn_6O_2(O_2CMe)_6(dpd)_3)]^{2+}$ (**4**; $dpdH_2$ = 1,3-di(pyridin-2-yl)-propane-1,3-dione dioxime) (Fig. 1). The $\{Mn^{III}_3(\mu_3\text{-}O^{2-})\}^{7+}$ unit of **3** is structurally very similar to monomer **2**, as is that of **4**, showing little perturbation from the linkage; most core parameters are identical within the 3σ criterion, or nearly so. The biggest variation is found in the Mn–N–O–Mn torsion angles. The Mn_3 triangle of **2** is clearly isosceles while those of **3**/**4** are equilateral, but it is not clear whether the crystallographic D_3 symmetry at each site of **3**/**4** is masking a lower local Mn_3 site symmetry such as isosceles, or whether the lower symmetry lattice of **2** (monoclinic $P2_1/c$) is causing a Mn_3 distortion to isosceles and those of **3**/**4** are truly equilateral. This point will be addressed further in the magnetic analysis (*vide infra*).

Magnetochemistry

Direct current magnetic susceptibility studies

There are two crucial questions to be addressed: (i) is each Mn_3 subunit within the cation of **3** still an SMM with $S = 6$, or has the oligomerization changed the magnetic properties compared with **2**? and (ii) is there any evidence for weak inter-Mn_3 interactions within the $[Mn_3]_2$ dimer cation?

To answer the first question, variable-temperature, solid-state dc magnetic susceptibility (χ_M) data were collected on samples, restrained in eicosane to prevent torquing, in an applied field of 1000 G (0.10 T) and in the 5.0–300 K temperature range. Given the crystallographic D_3 symmetry, the χ_MT *vs.* T data should be able to be fit to an equilateral Mn_3 triangle model, *i.e.*, a single J exchange constant. However, given the large amount of solvent in the crystal, we suspected that vacuum-drying might cause lowering of the local symmetry at each Mn_3 requiring the use of an isosceles triangle model, *i.e.*, with two exchange constants J and J', as we have employed before for Mn_3 monomer **2** and others with no crystallographic symmetry and a clear isosceles triangle structure.[41,61–63] We thus collected data on both air-dried and vacuum-dried samples (see Experimental section) and they are shown in Fig. 3.

For vacuum-dried **3**·$6H_2O$, χ_MT increases steadily from 25.39 cm^3 K mol^{-1} at 300 K to a peak value of 40.18 cm^3 K mol^{-1} at 25 K before decreasing slightly to 39.25 cm^3 K mol^{-1} at 5.0 K. The overall profile is very similar to that of monomer **2**, indicating that the two Mn_3 units within the dimer of **3**·$6H_2O$ are still ferromagnetically coupled, each with $S = 6$ ground states. The χ_MT value at 300 K is significantly higher than the expected spin-only ($g = 2.0$) value of 18.00 cm^3 K mol^{-1} for six Mn^{III} ($s = 2$; lowercase symbols are employed here to differentiate from the model used later to couple two giant spin SMMs within the $[Mn_3]_2$ dimers with total spin $S = 6$) non-interacting ions, suggesting that the **F** coupling within each Mn_3 unit shows up even at room temperature. The peak value at 25 K is as expected for two non-interacting $S = 6$ units with g slightly less than 2.0 (χ_MT = 42 cm^3 K mol^{-1} per $[Mn_3]_2$ with $g = 2.0$). The small drop below 25 K is assigned to ZFS and Zeeman effects.

Since the peak value at 25 K is what is expected for two Mn_3 units in their $S = 6$ ground states, it was assumed that to a first approximation the effects of ZFS on the 25–300 K data could be ignored. Thus, the data in the 25–300 K range above the peak were fit to the Van Vleck equation[49,64] for an equilateral triangle based on the isotropic Heisenberg spin Hamiltonian of eqn (2), where $s_1 = s_2 = s_3 = 2$ are the spins of each individual Mn^{III} ion.

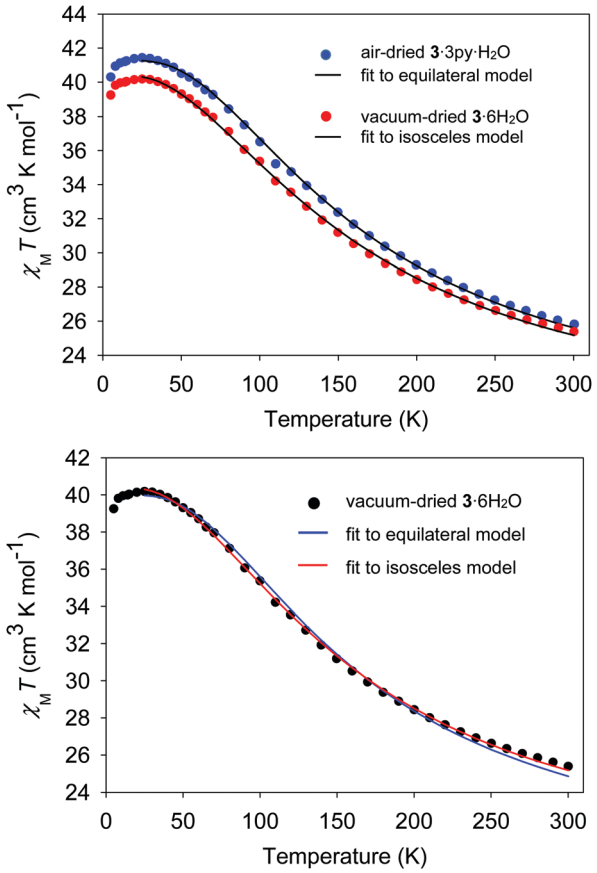

Fig. 3 (top) χ_MT per $[Mn_3]_2$ dimer *vs.* T for air-dried **3**·3py·H_2O and vacuum-dried **3**·$6H_2O$ samples in a 0.1 T dc field. The solid lines are the fits of the 25–300 K data to equilateral (single J) and isosceles (two J's) models. See the text for the fit parameters. (bottom) Comparison of the fits of χ_MT per $[Mn_3]_2$ dimer *vs.* T data for vacuum-dried **3**·$6H_2O$ to an equilateral *vs.* an isosceles triangle model. See the text for the fit parameters.

$$\hat{H} = -2J[\hat{s}_1\cdot\hat{s}_2 + \hat{s}_1\cdot\hat{s}_3 + \hat{s}_2\cdot\hat{s}_3] \quad (2)$$

The best fit (solid blue line in Fig. 3, bottom), which was of fair quality, gave J = +10.1(1) cm^{-1} and g = 1.95(1), with a constant temperature-independent paramagnetism (TIP) of 600×10^{-6} cm^3 mol^{-1}. We thus then fit the 25–300 K data to an isosceles model (eqn (3)), as used previously for monomer **2** and other $[Mn_3]_n$ complexes,[41,43,57,61]

$$\hat{H} = -2J[\hat{s}_1\cdot\hat{s}_2 + \hat{s}_1\cdot\hat{s}_3] - 2J'[\hat{s}_2\cdot\hat{s}_3] \quad (3)$$

and this gave a good fit (solid red line in Fig. 3) with J = +6.9(4) cm^{-1}, J' = +18.1(5) cm^{-1} and g = 1.96(1), with TIP again held constant at 600×10^{-6} cm^3 mol^{-1}. The root-mean-square J *vs.* J' error surface for the fit (Fig. S3 of ESI†) shows a second minimum of nearly equal quality with J = +14.5(4) cm^{-1}, J' = +2.7(4) cm^{-1}, and g = 1.96(1). We interpret the two fits as the two different distortions from equilateral to isosceles

(short-short-long and short-long-long Mn···Mn edges) and thus should be related, and in fact both have average J_{av} = +10.6 cm^{-1}.

For air-dried **3**·3py·H_2O, $\chi_M T$ increases steadily from 25.81 cm^3 K mol^{-1} at 300 K to a peak value of 41.44 cm^3 K mol^{-1} at 25 K before decreasing slightly to 40.30 cm^3 K mol^{-1} at 5.0 K. It has a steeper profile than the vacuum-dried sample, and this time a very good fit was obtained to the equilateral triangle model (solid line in Fig. 3, top) with J = +10.1(2) cm^{-1} and g = 1.98(1), with TIP = 600 × 10^{-6} cm^3 mol^{-1}. When the data for air-dried **3**·3py·H_2O were fit to the isosceles model, a slightly better fit was obtained, with J = +13.1(4) cm^{-1}, J' = +4.7(3) cm^{-1} (J_{av} = 10.3(4) cm^{-1}) and g = 1.98(1) (Fig. S4 of ESI†). We conclude that vacuum-drying removes the large amount of CH_2Cl_2 and py solvent from the **3**·3py·12CH_2Cl_2 crystals and causes the local structure of each Mn_3 to decrease below C_3, giving only a fair fit to the equilateral model. The volatile CH_2Cl_2 still all leaves during air-drying, but the milder drying conditions and retention of the py leads to a better fit to the equilateral model, which we interpret as due to a smaller structural perturbation. Unfortunately, the CH_2Cl_2 leaves too quickly for us to be able to collect data on pristine **3**·3py·12CH_2Cl_2 crystals. The resulting spin state energy diagrams for the two fits of **3**·3py·H_2O are shown in Fig. S5 (ESI†): for the equilateral model, the S_T = 5 and S_T = 4 first and second excited states, respectively, are at 121 and 222 cm^{-1} above the S_T = 6 ground state; in the isosceles model, the two S_T = 5 states are no longer degenerate and the first and second excited states are both S_T = 5 at 90 and 157 cm^{-1}, respectively, above the ground state.

To rule out the possibility that the fits to dc susceptibility data could be influenced by 2nd-order axial ZFS associated with the Mn^{III} ions, we additionally fit the data in the whole 5.0–300 K range to a model that includes both exchange and single-ion anisotropy, the latter calculated from the angle between the Mn^{III} JT axes and the Mn_3 easy-axis (z-axis) perpendicular to the Mn_3 plane (Fig. S6, ESI†). This procedure, which has its own limitations, is described in more detail in the ESI.† The main point to note here is that these fits yield values for the exchange parameters that are the same as those deduced from the exchange-only model, to within the associated uncertainties. The obtained curves differ only at low temperatures, where the effects of ZFS are most pronounced, and are essentially superimposable above 40 K with the fits of 25–300 K data that do not include ZFS.

To confirm the ground state of each Mn_3 sub-unit and to obtain an initial estimate of the molecular axial zero-field splitting parameter, D, we then addressed only the lowest T regime by collecting magnetization (M) *versus* field data in the 0.1–7.0 T and 1.8–10.0 K ranges. The data, plotted as $M/N\mu_B$ *vs.* $\mu_0 H/T$ in Fig. 4, where N is Avogadro's number, μ_B is the Bohr magneton, and μ_0 is the vacuum permeability, were fit with program MAGNET[54] by diagonalization of the giant spin Hamiltonian matrix assuming only the S = 6 ground state is populated, incorporating uniaxial anisotropy ($D\hat{S}_z^2$) and the Zeeman interaction associated with the applied field ($g\mu_B\mu_0\hat{S}\cdot\vec{H}$), and employing a full powder average (eqn (4)); $\hat{S}_z$ is the easy- (z-) axis spin

$$\hat{H} = D\hat{S}_z^2 + g\mu_B\mu_0\hat{S}\cdot\vec{H} \quad (4)$$

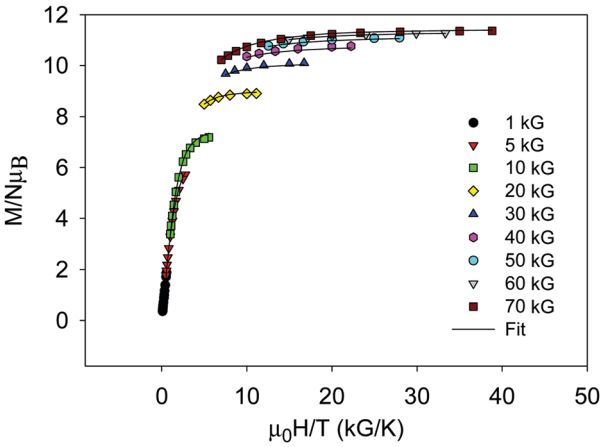

Fig. 4 Magnetization (M) per Mn_3 unit of **3**·6H_2O plotted as $M/N\mu_B$ *vs.* $\mu_0 H/T$. Solid lines are the fit of the data; see the text for the fit parameters.

operator. We again assumed each Mn_3 is acting independently, *i.e.*, any inter-Mn_3 interactions through 1,3-ppmd^{2-} linkers and other pathways are too weak to create a noticeable effect at these fields and temperatures. An excellent fit was obtained with S = 6, D = −0.32(2) cm^{-1}, and g = 1.95(2) (solid lines in Fig. 4). The g *vs.* D error surface (Fig. S7 of ESI†) shows another minimum with positive D but of much poorer quality. The negative D parameter is very similar to that obtained for **2** (S = 6, D = −0.34(2) cm^{-1}, and g = 1.92(2)), and in good agreement with the more accurate EPR measurements described below. We therefore see here that the low-temperature magnetic measurements provide reliable estimates of the spin Hamiltonian parameters associated with the ground state of the Mn_3 SMM, without dependence on the intra-molecular exchange, in the same way that the high-temperature (> 25 K) data constrain the J parameters without dependence on the ZFS interactions.

Alternating current (ac) magnetic susceptibility studies

As an independent probe of the ground state of each Mn_3 unit, and the magnitude and sign of a possible intra-dimer exchange interaction between them, ac magnetic susceptibility data on **3**·6H_2O were collected in the 1.8–15 K range in a 3.5 G ac field at oscillation frequencies of 50–1000 Hz. The in-phase ac susceptibility (χ'_M, plotted as $\chi'_M T$) is essentially constant with decreasing T at ∼41 cm^3 K mol^{-1} (Fig. 5, top), consistent with the sum expected for two independent S = 6 Mn_3 units with g slightly less than 2.0 (spin-only $\chi'_M T$ = 42 cm^3 K mol^{-1}) and no low-lying excited states. The constant $\chi'_M T$ also indicates that any exchange interaction between them is too weak to show up above 1.8 K, which is in contrast to the previous $[Mn_3]_2$ dimer with dpd^{2-} linkers, $[Mn_6O_2(O_2CMe)_6(dpd)_3](ClO_4)_2$ (**4**) that exhibited a gradual increase in $\chi'_M T$ below 15 K, clearly indicating an inter-Mn_3 **F** interaction (Fig. S8 of ESI†). Thus, as expected, the inter-Mn_3 coupling in **3** is weaker than in the dpd^{2-}-linked dimer **4** owing to the longer separation between oximate groups (Fig. S9 of ESI†), but it was possible that it might still show up below 1.8 K and be **F** as predicted based on the 1,3-phenylene unit in 1,3-ppmd^{2-}. Below ∼3 K, there is a frequency-dependent

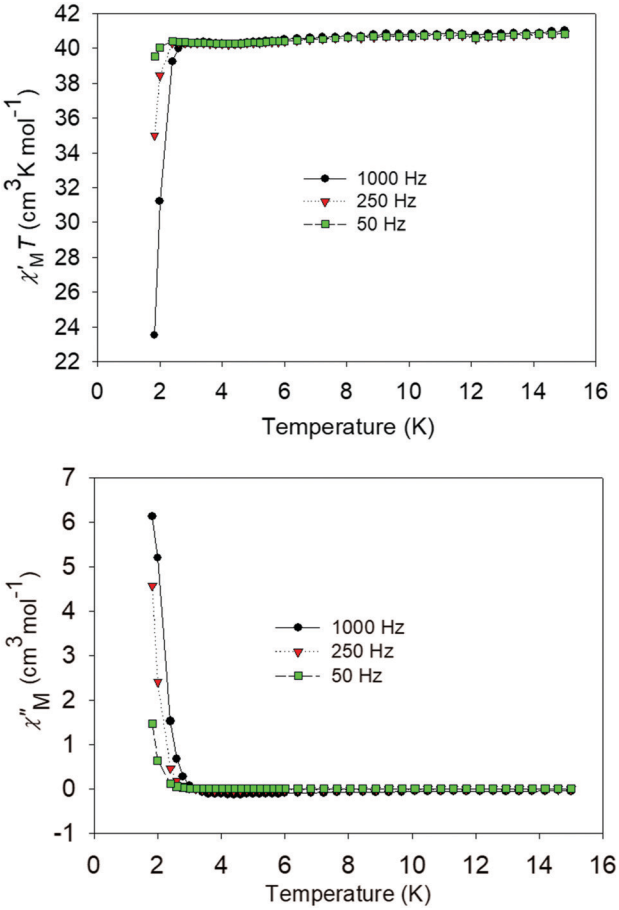

Fig. 5 Plots of the (top) in-phase (χ'_M, as $\chi'_M T$) and (bottom) out-of-phase (χ''_M) ac susceptibility data *vs.* T for **3**·6H$_2$O in a 3.5 G field at the indicated oscillation frequencies.

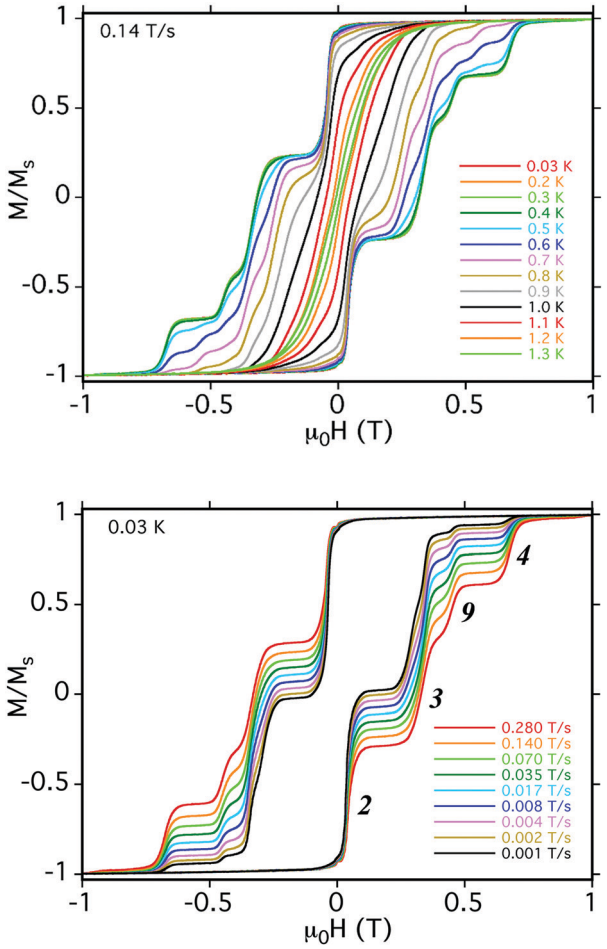

Fig. 6 Magnetization (M) *vs.* dc field hysteresis loops for a single crystal of **3**·3py·12CH$_2$Cl$_2$ (top) at the indicated temperatures at a 0.14 T s^{-1} field scan rate, and (bottom) at the indicated scan rates at 0.03 K. M is normalized to its saturation value, M_S. The step labels in the bottom figure refer to the QTM transitions in Table 3.

decrease in $\chi'_M T$ and an increase in the out-of-phase χ''_M signal (Fig. 5) indicative of the slow relaxation of an SMM.

Magnetization hysteresis and decay studies

Magnetization *vs.* dc field scans on a single crystal of **3**·3py·12CH$_2$Cl$_2$ freshly removed from mother liquor were carried out using a micro-SQUID[44] apparatus at sweep rates in the 0.001–0.280 T s^{-1} range with the field applied parallel to the magnetic easy-axis of the $[Mn_3]_2$ dimers, between temperatures of 0.03 and 1.3 K. Hysteresis loops were observed below 1.3 K (Fig. 6) whose coercivities increase with decreasing temperature and increasing field sweep rate, as expected for SMMs. The loops also exhibit steps characteristic of QTM. The blocking temperature is ~1.3 K, above which M relaxes faster than the time scale of the hysteresis measurement. Thus, each of the Mn_3 units in the $[Mn_3]_2$ dimer is an SMM, as previously found for monomer **2**, which they closely resemble in structure, spin and anisotropy.

Before analysing the features in the hysteresis loops, we describe the magnetization *vs.* time decay studies to characterize the relaxation dynamics. A large dc field was applied to the crystal at ~5 K to saturate the magnetization in one direction, the T decreased to a desired value in the 0.03–1.3 K range, and the field then removed and the M measured as a function of time (Fig. 7, inset). The relaxation time (τ) *vs.* T data obtained from these measurements were used to construct an Arrhenius plot (Fig. 7) based on eqn (5), where U_{eff} is the

$$\ln(\tau) = \ln(\tau_0) + U_{eff}/kT \quad (5)$$

effective barrier to magnetization relaxation and k is the Boltzmann constant. Below ~0.2 K, τ becomes temperature-independent as all relaxation is now by QTM *via* the lowest energy $m_S = \pm 6$ levels of the ground state $S = 6$ manifold.[5] The fit to the thermally activated region (dashed line in Fig. 7) gives $\tau_0 = 8 \times 10^{-7}$ s and $U_{eff} = 9.74$ cm^{-1} = 14.0 K. As expected, U_{eff} is smaller due to QTM than the theoretical barrier $U = 10.5$ cm^{-1} = 15.1 K, calculated by using the ZFS parameters determined from EPR data (*vide infra*).

We now address whether there is any interaction between the two Mn_3 SMM units within the dimer. The answer is yes because there is a clear exchange-bias effect visible in the hysteresis loops showing up as a shift of the first QTM step away from zero field. Monomer **2**, for example, shows a QTM

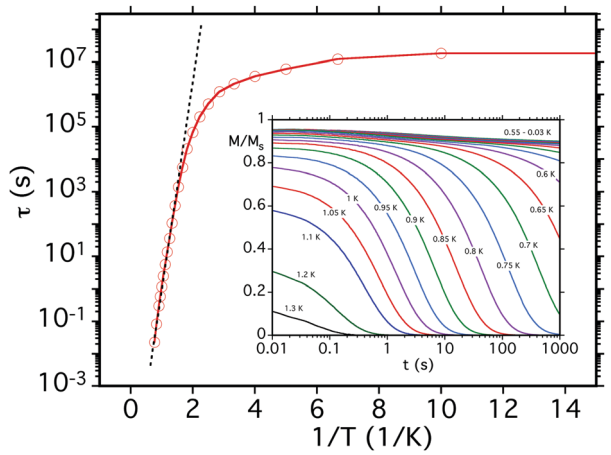

Fig. 7 Relaxation time (τ) *vs.* $1/T$ plot for a single crystal of **3**·3py·12CH_2Cl_2 obtained from the dc magnetization decay *vs.* time data in zero applied field at the indicated temperatures shown in the inset. The dashed line is the fit of the thermally-activated region to the Arrhenius equation. See the text for the fit parameters.

step at zero field as m_S states of the $S = 6$ spin manifold on one side of the anisotropy barrier are degenerate with m_S states on the other side.[57] Exchange coupling to a neighbouring SMM provides a source of a bias field that shifts the QTM step away from zero by an amount proportional to the coupling strength. Normally this inter-SMM coupling is **AF** and causes a negative shift, *i.e.*, the step appears before the scan reaches zero field,[21,41] but for **3**·3py·12CH_2Cl_2 the shift is clearly after zero field indicating a positive exchange bias field, of $H_{ex} = +0.06$ T, from a weak **F** inter-Mn_3 coupling.

This is the first time we have seen a positive exchange bias for the $[Mn_3]_n$ (n = 2, 4) SMM oligomers, and so we have analysed the system in detail. At these low temperatures, each Mn_3 unit can be modelled as a giant spin of $S = 6$, and the spin Hamiltonian ($\hat{H}_i$) for each Mn_3 SMM with Ising-like anisotropy is thus given by eqn (6),

$$\hat{H}_i = D\hat{S}_{zi}^{\,2} + \hat{H}_{\mathrm{trans},i} + g\mu_B\mu_0\hat{S}_{zi}\cdot H_z \qquad (6)$$

where i = 1 and 2 refer to the two Mn_3 units of the dimer, and H_z is the applied field along the molecular easy- (z-) axis. The first term accounts for the axial 2nd order ZFS, and the last term is the Zeeman interaction. The associated parameters, D and g, are assumed to be identical for the two halves of the dimer due to their symmetry equivalence. Meanwhile, the 2nd term denotes transverse ZFS terms that do not commute with $\hat{S}_z$ and are, therefore, responsible for the QTM. The exact form of this term is not important here, as discussed further below. The spin Hamiltonian for the complete $[Mn_3]_2$ dimer is then given by eqn (7),

$$\hat{H} = \hat{H}_1 + \hat{H}_2 - 2J_{12}\hat{S}_1\cdot\hat{S}_2 \qquad (7)$$

where $\hat{H}_1$ and $\hat{H}_2$ are the Hamiltonians from eqn (6), $S_1 = S_2 = 6$, and J_{12} is the exchange interaction between the two Mn_3 units.[65] Tunnelling among the $(2S + 1)^2 = 169$ energy states is allowed by the transverse anisotropy, $\hat{H}_{\mathrm{trans},i}$, and the transverse coupling terms containing the $\hat{S}_{xi}$ and $\hat{S}_{yi}$ operators.

The energy eigenvalues of $[Mn_3]_2$ can be calculated by exact diagonalization of eqn (7), although this is computationally demanding. However, due to its large spin, the low-lying energy states are overwhelmingly dictated by the axial terms in eqn (6) and (7), *i.e.*, those containing $\hat{S}_{zi}$, so long as the applied field is parallel to z. By contrast, the off-diagonal terms, $\hat{H}_{\mathrm{trans},i}$ and the $-2J_{12}\{\hat{S}_{x1}\hat{S}_{x2} + \hat{S}_{y1}\hat{S}_{y2}\}$ component of the exchange interaction, manifest as 1st order perturbations that only influence the low-lying states in the immediate vicinity of level-crossings, resulting in minute ($\sim$Hz to kHz) tunnel splittings (avoided level crossings). In other words, the exact forms of the transverse interactions are not important in accurately predicting the positions of QTM resonances. We thus employ eqn (8), which ignores all off-diagonal interaction terms. An added advantage of this approach is that the Hamiltonian is now diagonal in the $\hat{S}_{zi}$ basis and the spin projection quantum numbers (m_{S1}, m_{S2}) are exact. Consequently, one can derive a straightforward algebraic expression for the low-lying energy eigenvalues for the two Mn_3 SMMs in terms of their associated spin projections, $m_{Si} = \pm6, \pm5$, *etc.*, as given by eqn (9).

$$\hat{H} \approx \hat{H}_1 + \hat{H}_2 - 2J_{12}\hat{S}_{z1}\cdot\hat{S}_{z2} \qquad (8)$$

$$E = D(m_{S1}^{\,2} + m_{S2}^{\,2}) + g\mu_B\mu_0H_z(m_{S1} + m_{S2}) - 2J_{12}m_{S1}m_{S2} \qquad (9)$$

A spin-state energy *vs.* applied dc field plot based on eqn (9) is shown in Fig. 8 (top), whose parameters J_{12} and D have been adjusted to simulate the hysteresis loops by predicting QTM steps at the experimentally observed positions, giving $J_{12} = +4.5 \times 10^{-3}$ cm^{-1} = +6.5 mK ($\hat{H} = -2J_{12}\hat{S}_1\cdot\hat{S}_2$ convention) and $D = -0.35$ cm^{-1} = −0.50 K. It should be noted that this procedure is sensitive only to the Ising ($\hat{S}_{z1}\hat{S}_{z2}$) component of the exchange interaction, and therefore we cannot determine the exact form of the intra-dimer exchange interaction, *i.e.*, whether it is isotropic or anisotropic. We can now rationalize the hysteresis loops and QTM step positions.

At very low temperature, only the lowest-lying states are populated and involved in the QTM events, and an expansion of this region is therefore shown in Fig. 8 (bottom). As the field is swept from −1.0 T, where all dimers have been polarized into the (m_{S1}, m_{S2}) = (−6, −6) state, the first avoided level crossing is at 0.0 T (Table 3, crossing point **1**) where tunnelling from (−6, −6) to (+6, +6) could occur, but this requires both Mn_3 spins to tunnel simultaneously. Such a double quantum transition has a very small probability and is not seen. At the next avoided level crossing at +0.06 T (crossing point **2**), tunnelling can occur from (−6, −6) to (+6, −6), a single tunnelling transition, and a QTM step is seen; +0.06 T thus corresponds to the total bias field from the $m_S = -6$ neighbour. Note that (−6, −6) to (−6, +6) can also occur at this point, but for convenience we do not list in Fig. 8 (bottom) or Table 3 both degenerate (m_S, m'_S) and (m'_S, m_S) states. For those dimers that did tunnel at position **2**, the next avoided level crossing is at +0.31 T (crossing point **3**) where $[Mn_3]_2$ can undergo tunnelling

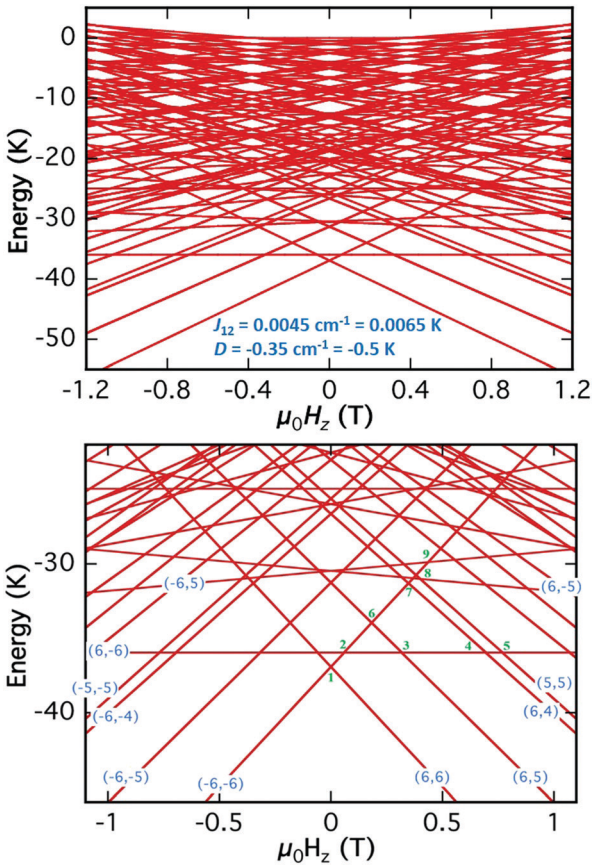

Fig. 8 (Top) Spin state energies *vs.* applied dc field plot for **3**·3py·12CH_2Cl_2 constructed with J = +4.5 × 10^{-3} cm^{-1} ($\hat{H} = -2J_{12}\hat{S}_1\cdot\hat{S}_2$ convention) and D = −0.35 cm^{-1} to simulate the positions of the avoided level crossings that lead to the experimentally observed QTM step positions in the hysteresis loops of Fig. 6. (Bottom) Expansion showing only the lower energy spin states populated at very low temperature, and the avoided level crossings relevant to the hysteresis loops in Fig. 6 when the field is swept from −1.2 T to +1.2 T. The green numbers **1** to **9** are the crossings listed in Table 3. Spin states are labelled in blue as (m_{S1}, m_{S2}) for the two Mn_3 units. See the text for the discussion of the avoided level crossings leading to the observed QTM steps in Fig. 6.

Table 3 Avoided level crossings giving QTM steps in the hysteresis loops of **3**·3py·12CH_2Cl_2

Crossing[a]	Transition	Type[b]	Observed?
1	(−6, −6) → (+6, +6)	Double	No
2	(−6, −6) → (+6, −6)	Single	+0.06 T
3	(+6, −6) → (+6, +5)	Single	+0.31 T
4	(+6, −6) → (+6, +4)	Single	+0.68 T
5	(+6, −6) → (+5, +5)	Double	No
6	(−6, −6) → (+6, +5)	Double	No
7	(−6, −6) → (+6, +4)	Double	No
8	(−6, −6) → (+5, +5)	Double	No
9	(−6, −6) → (−6, +5)	Single	+0.43 T
10	(+6, −6) → (+6, +6)	Single	−0.06 T
11	(+6, −6) → (−5, −6)[c]	Single	−0.31 T
12	(+6, −6) → (−4, −6)[d]	Single	−0.68 T
13	(+6, +6) → (+6, −5)	Single	−0.43 T

[a] Numbered as in Fig. 8 and 9. [b] Single or double quantum transition. [c] Degenerate with (−6, −5). [d] Degenerate with (−6, −4).

from (+6, −6) to the (+6, +5) excited state, which will then relax to the (+6, +6) ground state. Those molecules that did not tunnel at position **3** can next do so at +0.68 T (crossing point **4**) from (+6, −6) to the (+6, +4) excited state, followed by relaxation to (+6, +6). For those molecules that did not tunnel at position **2**, the next crossing that does not involve a double tunnelling transition is at +0.43 T (crossing point **9**) where tunnelling from (−6, −6) to the (−6, +5) excited state occurs, followed by relaxation. Other marked level crossings in the 0.10–0.80 T range, at positions **5**, **6**, **7** and **8**, are all double quantum transitions and are not seen. This analysis thus predicts that there should be four QTM steps, arising from the tunnelling transitions at positions **2**, **3**, **4**, and **9**, in agreement with the hysteresis loops in Fig. 6 (bottom).

We can now also explain other features of the hysteresis loops: At a slow 0.001 T s^{-1} scan rate at 0.03 K, the spin S is 'in resonance' between two states at avoided level crossing **2** for a longer time and almost all molecules tunnel to (+6, −6) leading to $M/M_S \approx 0$ and a large QTM step, and then again to (+6, +5) at crossing **3** giving another large step. This is as expected from standard Landau–Zener theory,[66] which predicts that the tunnelling probability increases with decreasing field scan rate. As a result, there are few molecules left to tunnel at crossings **9** and **4**, and small QTM steps are thus seen at both positions. As the scan rate is increased up to 0.28 T s^{-1}, the proportion of molecules that tunnel at crossings **2** and **3** progressively decreases, and the QTM steps thus become smaller and smaller, whereas there are more molecules left to tunnel at crossings **9** and **4** and these steps become progressively larger.

We also performed minor-loop scans by sweeping at 0.03 K from −1 T to various fields and then reversing the sweep direction, the objectives being twofold: to test the validity of the model and Fig. 8, and directly obtain J_{12} and D from the loops rather than just from the simulation. The strategy is summarized in Fig. 9 (top) and involves scanning through avoided level crossing **2** at +0.06 T to allow some molecules to tunnel from (−6, −6) to (+6, −6) (or its (−6, +6) degenerate partner), and then reversing the sweep direction. At avoided crossing **10**, some molecules will tunnel to the (+6, +6) state and the next crossing that can lead to a single tunnelling transition and QTM step is at position **13** involving (+6, +6) → (+6, −5), followed by relaxation to (+6, −6) (blue arrow in Fig. 9, top). Molecules that do not tunnel at position **10** can instead do so at position **11** to (−5, −6) followed by relaxation to (−6, −6), and those that do not can then tunnel at position **12** to (−4, −6), followed by relaxation. The field positions of QTM steps **2**, **11**, **12**, and **13** can be used to determine J_{12} and D, as shown in Fig. 9 (top). The experimental minor-loop scans obtained at 0.14 T s^{-1} clearly show these steps (Fig. 9, bottom). The **2**/**11** and **11**/**12** field separations of $\mu_0\Delta H \approx 0.37$ T obtained from Fig. 9 (bottom, inset) and the use of eqn (10) give $D \approx -0.35(3)$ cm^{-1} with g = 2.0, in agreement with the D value from the simulation (Fig. 8) and within uncertainty

$$|D| = g\mu_B\mu_0\Delta H \quad (10)$$

with that from the magnetization fit (Fig. 4). Further, the **11**/**13** field separation depends on $2J_{12}$, and a field separation of

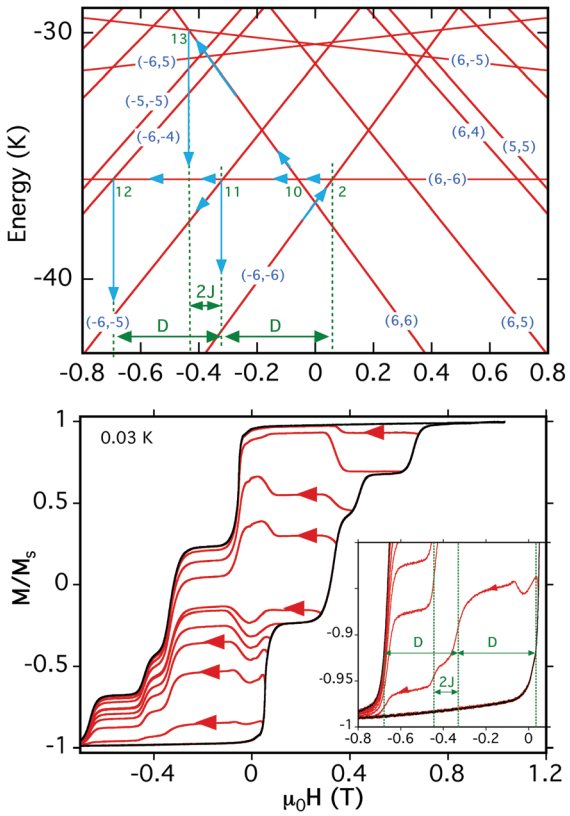

Fig. 9 (Top) Portion of the spin state energy plot of Fig. 8, bottom, showing the minor loop strategy of scanning the dc field from −1 T to past crossing **2** and then reversing the scan (blue chevrons). Avoided level crossings **10** to **13** are those listed in Table 3 that should lead to QTM steps. Blue arrows show thermal relaxations after QTM from the generated excited states. Green arrows show the targeted field separations between QTM steps to obtain J (= J_{12}) and D. (Bottom) Experimental minor loop scans at 0.03 K and a 0.14 T s^{-1} dc field sweep rate showing the targeted QTM steps. The inset shows the clear observation of the QTM steps resulting from the avoided level crossings **2** and **11** to **13**, and the measurement of the ΔH used to obtain J_{12} and D; see the text for details.

$\mu_0\Delta H_{ex} \approx 0.12$ T (twice the exchange-bias field) obtained from Fig. 9 (bottom, inset) and use of eqn (11) ($\hat{H} = -2J_{12}\hat{S}_1\cdot\hat{S}_2$ convention)[67,68] gave

$$\mu_0\Delta H_{ex} = \frac{2J_{12}S}{g\mu_B} \qquad (11)$$

$J_{12} \approx +4.7(3) \times 10^{-3}$ cm^{-1} (+6.7(5) mK) for a spin of $S = 6$, in agreement within experimental uncertainty with the simulation values. Measuring the same field positions in the simulation (Fig. 8, bottom) gives essentially identical values of D and J_{12}, thus supporting the overall validity of the model employed and the overall analysis of the hysteresis loops.

High-field electron paramagnetic resonance (HFEPR) studies

HFEPR measurements were performed on a finely ground powder sample of **3**·3py·H_2O, primarily to determine the full spin Hamiltonian parameterization for the individual Mn_3 SMM units, while also providing additional information about the weak inter-Mn_3 exchange coupling. Experimental spectra recorded at a microwave frequency of 270 GHz are displayed as a function of temperature in Fig. 10a. Several distinct resonant features can be seen, which have been labelled according to the scheme shown in the inset. The peaks on the low-field side of the $g = 2.00$ position (9.64 T), labelled z_1 to z_4, correspond to turning points in the powder pattern such that the applied field is parallel to the molecular easy-, or z-axis. Within the uncoupled basis ($J_{12} = 0$), these resonances correspond to transitions associated with the individual $S = 6$ Mn_3 units from $m_S = -6$ to -5 (z_1), $m_S = -5$ to -4 (z_2), and so on, as depicted in the left-hand panel of the inset. Meanwhile, the broad dip on the high-field side of $g = 2.00$ corresponds to turning points of the powder pattern for the applied field in the molecular hard-, or xy-plane. The peak just to the left of z_1, labelled HF, is assigned as a half-field transition. These are typically seen in powder HFEPR spectra, even for highly axial systems, because transverse components of the Zeeman interaction induce otherwise forbidden $\Delta m_S = \pm 2$ transitions that are prominent in the isotropic $g = 4.00$ half-field region of the spectrum.

In order to explain the experimental results, we adopt a model that is very similar to the one used to explain the magnetization hysteresis measurements. However, the uneven spacing of the peaks labelled z_1 to z_4 requires inclusion of a fourth-order axial ZFS interaction, which is well documented in similar Mn_3 triangles.[69–71] We therefore modify eqn (6) as shown in eqn (12).

$$\hat{H}_i = D\hat{S}_{zi}^2 + \hat{H}_{trans,i} + B_4^0\hat{O}_{4i}^0 + \mu_B\mu_0\hat{S}_i\cdot\vec{\vec{g}}\cdot\vec{H} \qquad (12)$$

Eqn (12) explicitly considers all possible applied field orientations through the $\vec{\vec{g}}$-tensor in the Zeeman term. Meanwhile the fourth order axial anisotropy at each site, i (= 1, 2), is expressed in terms of the extended Stevens operator (ESO, see Table 4), $\hat{O}_{4i}^0$, and the associated parameter, B_4^0.[56] As with the hysteresis measurements, we assume the ZFS parameters to be identical for the two halves of the dimer. Simulations of the experimental spectra can then be generated by combining eqn (12) with the coupled Hamiltonian of eqn (7). The best simulations of the combined HFEPR data set are included below each of the experimental spectra in Fig. 10a.

In order to account for the variations in linewidth and lack of resolution of the xy resonances, strain parameters, σ_D and σ_E, were also included in the simulations. The former expresses a Gaussian distribution in the 2nd order axial ZFS parameter, D, while the latter assumes a rhombic interaction, $\hat{H}_{trans,i} = E(\hat{S}_{xi}^2 - \hat{S}_{yi}^2)$, with a broad distribution centred at $E = 0$. The combined HFEPR parameter set is given in Table 4. The observed strains are clearly a manifestation of the disorder induced by the loss of the volatile CH_2Cl_2 solvent (and possibly also some of the py) upon drying and grinding of the powder sample. The intrinsic tilting of the Mn^{III} JT axes results in a situation in which each ion projects a sizeable magnetic anisotropy into the xy-plane, but the three transverse contributions within each Mn_3 unit exactly cancel (*i.e.*, $E = 0$) for the perfect equilateral geometry. Meanwhile, the axial ZFS (D) is significantly reduced relative to the theoretical maximum in which the JT axes

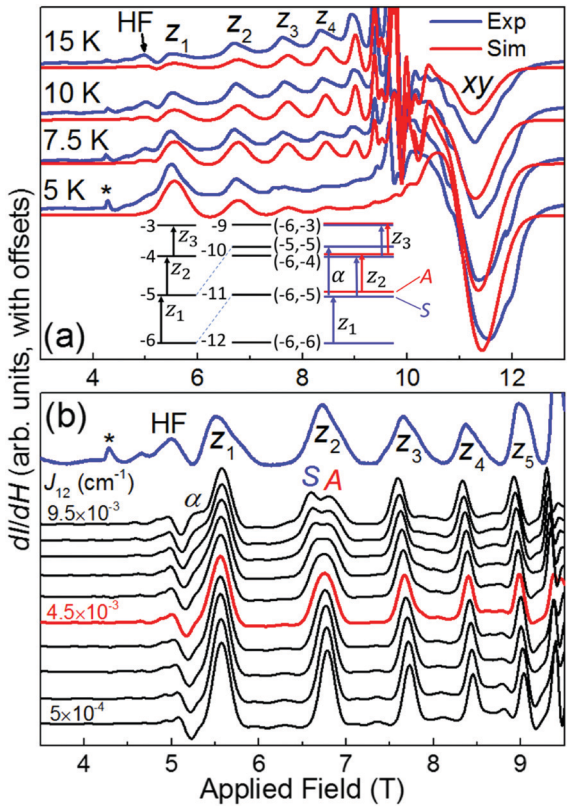

Fig. 10 (a) Experimental (Exp) and simulated (Sim) powder HFEPR spectra of **3**·3py·H_2O at a frequency of 270 GHz, plotted as d*I*/d*H* (*I* = transmitted intensity) for temperatures in the range from 5 to 15 K. The resonances labeled z_1 to z_4 correspond to the parallel (*z*-) components of the powder pattern, *xy* correspond to the perpendicular components, and HF is a half field transition (see main text for explanation); the feature labeled with an asterisk (*) corresponds to a known O_2 impurity in the sample holder. The inset schematically depicts the lowest lying energy levels appropriate to the parallel resonances. On the left are the uncoupled states associated with each individual S = 6 Mn_3 SMM, labeled according to m_S value, with the m_{S1},m_{S2} transitions corresponding to resonances z_1 to z_3 labeled. The middle panel shows the levels associated with the uncoupled dimer, labeled according to $|m_{S1},m_{S2}\rangle$; as can be seen, the new states are generated simply by exciting one of the spins, thereby translating (dashed lines) the overall energy of the dimer accordingly. The right panel depicts the fully coupled energy levels, labeled according to ($|m_{S2},m_{S1}\rangle$), where the blue and red states respectively correspond to the symmetric (*S*) and antisymmetric (*A*) combinations of $|m_{S1},m_{S2}\rangle$ and $|m_{S2},m_{S1}\rangle$. (b) Simulations of the 10 K spectrum as a function of the exchange coupling parameter, J_{12} (in steps of 10^{-3} cm^{-1}, see legend). The linewidth is reduced from the best simulations in (a) so that it is possible to resolve additional resonances that emerge due to the exchange coupling, *i.e.*, α and the *S* and *A* z_2 resonances. The red simulated spectrum corresponds to the value of J_{12} deduced from magnetic hysteresis experiments and the value used for the simulations in (a).

Table 4 Spin Hamiltonian parameters for individual Mn_3 SMM units in **3** from simulation of the combined powder HFEPR dataset using eqn (12) in combination with eqn (7) and assuming J_{12} = +4.5 × 10^{-3} cm^{-1} as determined from the magnetization hysteresis studies

Parameter	Value
D^a	−0.29(1) cm^{-1}
E^a	0
$B_4^{0\,b}$	−6.67(3) × 10^{-5} cm^{-1}
$\sigma_D{}^c$	0.028 cm^{-1}
$\sigma_E{}^c$	0.028 cm^{-1}
$g_{xy}{}^d$	1.98(1)
g_z	1.98(1)

[a] Mean value of the distribution, with associated uncertainty. [b] ZFS parameter associated with the ESO, $\hat{O}_4^0 = 35\hat{S}_z^4 - \{30S(S+1) - 25\}\hat{S}_z^2$. [c] Values correspond to the standard deviation of the Gaussian distribution. [d] Values constrained from ultra-high field EPR measurements (Fig. S10).

are aligned with the molecular C_3 axis. Disorder then results in local variations in the ZFS at each Mn^{III} site, both in magnitude and in the orientations of the tensors. First and foremost, this results in non-cancellation of the 2nd-order rhombic ZFS. However, the emergent distribution in *E* should be centered at zero, because the sign determines simply whether a given distortion is along *x* or *y*. Meanwhile, a similar distribution in *D* is anticipated because the JT axes are very severely tilted, such that the projections of the local Mn^{III} ZFS contributions along *z* and into the *xy*-plane are quite similar.

Attempts to constrain the exchange coupling parameter, J_{12}, proved unsuccessful due to relatively broad linewidths (primarily dictated by σ_D for the most resolved z_1 to z_4 resonances). Fig. 10b presents a series of simulations using the optimal HFEPR parameterization given in Table 4, while varying the magnitude of J_{12}. The linewidth was reduced ($\sigma_D = \sigma_E$ = 8.5 × 10^{-3} cm^{-1}) for these simulations in order to clearly resolve additional resonances that emerge due to the exchange coupling. The inset to Fig. 10a reveals the origin of these resonances: the middle panel depicts the relevant low-lying energy levels associated with the uncoupled states, but in a two-spin basis, (m_{S1}, m_{S2}), labelled according to the sum, $M = m_{S1} + m_{S2}$; meanwhile, the right-hand panel shows the fully coupled energy levels.[43] States for which $m_{S1} \neq m_{S2}$ are doubly degenerate in the uncoupled case ($J_{12} = 0$) and split into symmetric (*S*) and antisymmetric (*A*) combinations of the uncoupled states for finite exchange; the degree of splitting depends on the difference between m_{S1} and m_{S2}, being largest when $\Delta m_S = 1$, *e.g.*, for (−6, −5). States for which $m_{S1} = m_{S2}$ are singlets, although their energies do depend on J_{12}.[13,14]

As can be seen in Fig. 10b, the z_1 transition is unaffected by the exchange, even though the character of the excited state evolves into the $\{|-6,-5\rangle + |-5,-6\rangle\}$ symmetric combination. However, an additional resonance splits off from z_1 that we label α. In the uncoupled basis, this resonance corresponds to the case where one Mn_3 unit makes a transition from $m_S = -6$ to −5, while the other Mn_3 unit is in its first excited $m_S = -5$ state; it is degenerate with z_1 if $J_{12} = 0$ because the two halves of the dimer do not know about each other. However, in the finite J_{12} case, the degeneracy is broken and the α resonance ($|-6,-5\rangle_S$ to $|-5,-5\rangle_S$) emerges on the low-field side of z_1 with a weaker intensity because it originates from an excited state of the full dimer. By contrast, a much more obvious splitting of the z_2 resonance is seen in the presence of exchange, with the new/split resonances corresponding to transitions exclusively between either the symmetric (*S*) or antisymmetric (*A*) states;[43] the overall intensity shrinks because the original spectral weight

is divided among these two resonances. Although unresolved, even with the reduced strain parameter, the z_3, z_4, *etc.*, resonances also split into *A* and *S* doublets. Meanwhile, many of the peaks shift to lower field upon increasing J_{12} due to the associated exchange bias. However, it is not possible to constrain J_{12} from these shifts because the effect is similar to that of B_4^0. Unfortunately, as can be seen from comparisons with the actual spectra (top of Fig. 10b), the z_2 splitting (and the emergence of α) is well within the experimental linewidth for J_{12} values up to at least a factor of two larger than deduced from hysteresis measurements. Therefore, we conclude that the resolution of the HFEPR spectra does not permit evaluation of J_{12}. Previous HFEPR studies of related dimers were able to resolve exchange doublets arising from transitions between entangled states of the two subunits.[13,14,43] In spite of their absence in the present investigation, the HFEPR spectra are consistent with the hysteresis measurements and confirm the targeted weak intra-dimer exchange in **3**·3py·12CH_2Cl_2, which was the main aim of this work.

We conclude this section by noting that the mean EPR *D* parameter is slightly smaller than the one determined from the hysteresis measurements (eqn (10)). This is due to the different spin Hamiltonians employed in modelling the two experiments, *i.e.*, eqn (12) includes the 4th order axial ZFS interaction whereas eqn (6) does not. It is straightforward to show that the HFEPR parameterization correctly predicts the magnetic field spacing, $\mu_0\Delta H = 0.37$ T, between hysteresis loop steps **2** and **11** (see ESI†). In other words, the two parameter sets are fully compatible, but the two techniques vary in their sensitivity to the exchange and ZFS. Hence, the hysteresis measurements constrain J_{12}, while the HFEPR measurements provide the optimum 2nd and 4th-order axial ZFS parameters for the isolated Mn_3 SMM units; this illustrates the power of combining multiple spectroscopic techniques. It is also important to comment on the influence of the disorder on the ZFS parameterization. Although the HFEPR analysis indicates significant distributions in these parameters, the mean values are again entirely consistent across all measurements: note that the *D* parameter obtained from fits to dc magnetization data (for both vacuum- and air-dried solid) is the same as the one deduced from the QTM measurements, which is consistent with the HFEPR studies for the reasons explained above. In other words, the disorder simply perturbs the local molecular properties without significantly modifying the average properties. It is just that a spectroscopic technique such as HFEPR is exquisitely sensitive to such perturbations, whereas a bulk thermodynamic probe is not.

Origin of the inter-Mn_3 ferromagnetic coupling

Complex **3** is the first molecular aggregate of 3d SMMs to exhibit exchange-biased QTM steps from ferromagnetic inter-SMM coupling, and it is thus pertinent to ask what the mechanism of the **F** coupling is. Taking the JT axis as the local *z* axis at each near-octahedral Mn^{III} (d^4) ion, the σ-symmetry $d_{x^2-y^2}$ orbital is empty, and the d_{z^2} magnetic orbital points towards O atoms from an acetate and an oximate NO unit (green bonds in Fig. 2). This means that σ-spin delocalization along the σ-bonds of the 1,3-ppmd^{2-} linkers as the mechanism of the inter-Mn_3 interaction would involve ten σ-bonds and is therefore ruled out; in any case, σ-spin delocalization would be expected to give **AF** coupling. Instead the **F** coupling is proposed to arise from spin density getting into the oximate π system from overlap with the Mn d_π orbitals putting π-symmetry spin all the way up to the C atoms attached to the phenylene linker (Fig. 11). Then **F** coupling is expected, as mentioned in the introduction, as long recognized in the organic spin literature for radicals attached to the 1, 3 positions of a phenylene ring.[45,46] The rationalization here is that the π-spin density spin-polarizes the bonding pair of electrons in the C–C σ-bond whose propagation across four phenylene bonds leads to parallel alignment of the two ends, *i.e.*, a **F** J_{12}. A related spin polarization was proposed to explain the **F** J_{12} in **4**, and the fact that there it only involved two bonds also rationalizes the stronger $J_{12} = 0.025$ cm^{-1} for **4** compared with $J_{12} = 0.0045$ cm^{-1} for **3**, since spin polarization effects attenuate significantly with the number of bonds (Fig. S8 of ESI†). Note that the phenylene and two oximate π-systems of each 1,3-ppmd^{2-} are not conjugated: the two oximates are near-perpendicular ($\sim 80^\circ$) and the phenylene ring is $\sim 55^\circ$ to each one. Thus, J_{12} is unlikely to be mediated by π-spin delocalization involving the phenylene π-system. The triple layer of π-stacked aromatic rings involving the py solvent molecules mentioned earlier, however, may provide a very weak **AF** interaction to the observed J_{12}, weakening its positive value.

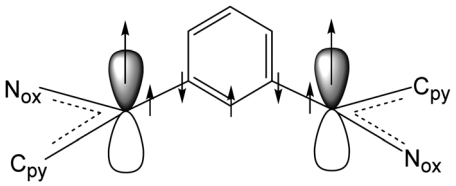

Fig. 11 The proposed contribution to the inter-Mn_3 ferromagnetic coupling by spin polarization of σ-bonding electrons to the central 1,3-phenylene unit of the 1,3-ppmd^{2-} linker by the spin density in the orthogonal π-system. N_{ox} = oximate N atom; C_{py} = 2-C atom of the pyridine ring.

It is also pertinent to consider whether the **F** coupling could perhaps result from simple through-space intramolecular dipolar interactions, as the obtained J_{12} parameter is rather weak. An exact calculation that considers the pairwise interactions between the three Mn^{III} ions on each half of the dimer arrives at a value of $J_d = 0.0021$ cm^{-1} (same $\hat{H} = -2J_d\hat{S}_{1z}\hat{S}_{2z}$ convention) for the dipolar coupling strength. This is too small to account for the magnitude of the observed exchange bias. However, it clearly contributes and will also impart some anisotropy to the overall coupling tensor, although the measurements reported here are insensitive to this anisotropy. Likewise, one could consider longer-range dipolar interactions, but this would result in a collective QTM behaviour that depended on the overall magnetization of the sample. However, the minor-loop strategy (Fig. 9) shows that the QTM step positions can be explained entirely on the basis of a single-molecule picture, regardless of the magnetization of the sample.

A related question is how can we be sure that the coupling is not between two Mn_3 units in different $[Mn_3]_2$ dimers? *i.e.* an inter-dimer interaction. If the linker was not the primary pathway of interaction between two Mn_3 units in neighbouring dimers,

then it would be instructive to compare inter-Mn_3 metric parameters in dimer **3**·3py·12CH_2Cl_2 with those in monomeric **2**·3CH_2Cl_2. The former's contacts with surrounding molecules are almost all with CH_2Cl_2 solvent molecules, except for a very few contacts involving C–H bonds from acetate groups to O atoms of the neighbouring dimer (C···O ≈ 3.5 Å). These almost certainly would lead to extremely weak **AF** interactions and, at best, may be serving to decrease the observed positive exchange-bias in **3**. In addition, **2**·3CH_2Cl_2 also contains intermolecular C–H···O contacts (C···O ≈ 3.6 Å) as well as significant inter-Mn_3 two-ring π-stacking interactions, and yet shows zero exchange bias of its QTM step at zero field. We thus conclude that the primary interactions between two Mn_3 units leading to the observed **F** exchange-bias are intra-dimer through the linker groups and partly through space, *i.e.*, dipolar.

Conclusions

A covalently-linked $[Mn_3]_2$ dimer of S = 6 SMMs has been targeted and achieved employing 1,3-ppmd^{2-}, a 'V-shaped' dioximate linker with a central 1,3-phenylene unit. The latter was chosen to target **F** inter-Mn_3 coupling, and this was confirmed by single-crystal magnetization *vs.* dc field scans below 1.3 K, which displayed QTM with a positive exchange bias. This has allowed a detailed analysis of the QTM transitions for a **F** dimer of SMMs to be accomplished for the first time. HFEPR studies have determined spin Hamiltonian parameters to fourth order for the individual Mn_3 SMM units of the $[Mn_3]_2$ dimer and provided an independent assessment of a very weak inter-Mn_3 interaction. The combined results emphasize the utility of a controlled means of linking SMMs, and by extension other magnetic molecules, with designed bifunctional linkers that can target weak intermolecular **F** or **AF** coupling, control that is important to develop in order to assess the potential of molecular spin-based oligomers for use as multi-qubits and/or other components in new quantum technologies.

Conflicts of interest

There are no conflicts to declare.

Acknowledgements

This study at the University of Florida and Florida State University was supported by the Center for Molecular Magnetic Quantum Materials, an Energy Frontier Research Center funded by the U.S. Department of Energy, Office of Science, Basic Energy Sciences under Award No. DE-SC0019330. HFEPR measurements were performed using instruments at the National High Magnetic Field Laboratory, which is supported by the National Science Foundation (DMR-1644779) and the State of Florida. We thank the NSF for funding of the X-ray diffractometer (grant CHE-1828064) and partial support of the synthetic studies (CHE-1565664). W. W. thanks the A. von Humboldt Foundation and the ERC for Grant MoQuOS 741276.

References

1 R. Sessoli, D. Gatteschi, A. Caneschi and M. A. Novak, *Nature*, 1993, **365**, 141–143.
2 R. Sessoli, H.-L. Tsai, A. R. Schake, S. Wang, J. B. Vincent, K. Folting, D. Gatteschi, G. Christou and D. N. Hendrickson, *J. Am. Chem. Soc.*, 1993, **115**, 1804–1816.
3 G. Christou, D. Gatteschi, D. N. Hendrickson and R. Sessoli, *MRS Bull.*, 2000, **25**, 66–71.
4 G. Christou, *Polyhedron*, 2005, **24**, 2065–2075.
5 R. Bagai and G. Christou, *Chem. Soc. Rev.*, 2009, **38**, 1011–1026.
6 L. Bogani and W. Wernsdorfer, *Nat. Mater.*, 2008, **7**, 179–186.
7 K. Katoh, H. Isshiki, T. Komeda and M. Yamashita, *Chem. – Asian J.*, 2012, **7**, 1154–1169.
8 J. R. Friedman, M. P. Sarachik, J. Tejada and R. Ziolo, *Phys. Rev. Lett.*, 1996, **76**, 3830–3833.
9 L. Thomas, F. Lionti, R. Ballou, D. Gatteschi, R. Sessoli and B. Barbara, *Nature*, 1996, **383**, 145–147.
10 W. Wernsdorfer and R. Sessoli, *Science*, 1999, **284**, 133–135.
11 W. Wernsdorfer, M. Soler, G. Christou and D. N. Hendrickson, *J. Appl. Phys.*, 2002, **91**, 7164–7166.
12 W. Wernsdorfer, N. E. Chakov and G. Christou, *Phys. Rev. Lett.*, 2005, **95**, 037203.
13 S. Hill, R. S. Edwards, N. Aliaga-Alcalde and G. Christou, *Science*, 2003, **302**, 1015–1018.
14 A. Wilson, S. Hill, R. S. Edwards, N. Aliaga-Alcalde and G. Christou, *AIP Conf. Proc.*, 2006, **850**, 1141–1142.
15 R. Tiron, W. Wernsdorfer, D. Foguet-Albiol, N. Aliaga-Alcalde and G. Christou, *Phys. Rev. Lett.*, 2003, **91**, 227203.
16 W. Wernsdorfer, S. Bhaduri, R. Tiron, D. N. Hendrickson and G. Christou, *Phys. Rev. Lett.*, 2002, **89**, 197201.
17 M. N. Leuenberger and D. Loss, *Nature*, 2001, **410**, 789–793.
18 A. Gaita-Ariño, F. Luis, S. Hill and E. Coronado, *Nat. Chem.*, 2019, **11**, 301–309.
19 (*a*) B. Zhou, R. Tao, S.-Q. Shen and J.-Q. Liang, *Phys. Rev. A: At., Mol., Opt. Phys.*, 2002, **66**, 010301; (*b*) M. Affronte, F. Troiani, A. Ghirri, A. Candini, M. Evangelisti, V. Corradini, S. Carretta, P. Santini, G. Amoretti, F. Tuna, G. Timco and R. E. P. Winpenny, *J. Phys. D: Appl. Phys.*, 2007, **40**, 2999–3004.
20 R. Vincent, S. Klyatskaya, M. Ruben, W. Wernsdorfer and F. Balestro, *Nature*, 2012, **488**, 357–360.
21 W. Wernsdorfer, N. Aliaga-Alcalde, D. N. Hendrickson and G. Christou, *Nature*, 2002, **416**, 406–409.
22 M. Murugesu, R. Clérac, W. Wernsdorfer, C. E. Anson and A. K. Powell, *Angew. Chem.*, 2005, **117**, 6836–6840.
23 C. Coulon, H. Miyasaka and R. Clérac, *Struct. Bond.*, 2006, **122**, 163–206.
24 T. Shiga, H. Miyasaka, M. Yamashita, M. Morimoto and M. Irie, *Dalton Trans.*, 2011, **40**, 2275.
25 G. Wu, J. Huang, L. Sun, J. Bai, G. Li, E. Cremades, E. Ruiz, R. Clérac and S. Qiu, *Inorg. Chem.*, 2011, **50**, 8580–8587.
26 I.-R. Jeon and R. Clérac, *Dalton Trans.*, 2012, **41**, 9569–9586.
27 Y. Liu, Z. Chen, J. Ren, X.-Q. Zhao, P. Cheng and B. Zhao, *Inorg. Chem.*, 2012, **51**, 7433–7435.
28 A. D. Katsenis, R. Inglis, A. Prescimone, E. K. Brechin and G. S. Papaefstathiou, *CrystEngComm*, 2012, **14**, 1216–1218.

29 D. P. Giannopoulos, A. Thuijs, W. Wernsdorfer, M. Pilkington, G. Christou and T. C. Stamatatos, *Chem. Commun.*, 2014, **50**, 779–781.
30 H. Miyasaka, K. Nakata, L. Lecren, C. Coulon, Y. Nakazawa, T. Fujisaki, K. I. Sugiura, M. Yamashita and R. Clérac, *J. Am. Chem. Soc.*, 2006, **128**, 3770–3783.
31 E. E. Moushi, T. C. Stamatatos, W. Wernsdorfer, V. Nastopoulos, G. Christou and A. J. Tasiopoulos, *Angew. Chem., Int. Ed.*, 2006, **45**, 7722–7725.
32 H. Miyasaka and M. Yamashita, *Dalton Trans.*, 2007, 399–406.
33 H.-B. Xu, B.-W. Wang, F. Pan, Z.-M. Wang and S. Gao, *Angew. Chem.*, 2007, **119**, 7532–7536.
34 L. Bogani, A. Vindigni, R. Sessoli and D. Gatteschi, *J. Mater. Chem.*, 2008, **18**, 4750–4758.
35 O. Roubeau and R. Clérac, *Eur. J. Inorg. Chem.*, 2008, 4325–4342.
36 L. F. Jones, A. Prescimone, M. Evangelisti and E. K. Brechin, *Chem. Commun.*, 2009, 2023–2025.
37 S. K. Langley, N. F. Chilton, B. Moubaraki and K. S. Murray, *Dalton Trans.*, 2011, **40**, 12201.
38 V. Bellini, G. Lorusso, A. Candini, W. Wernsdorfer, T. B. Faust, G. A. Timco, R. E. P. Winpenny and M. Affronte, *Phys. Rev. Lett.*, 2011, **106**, 227205.
39 A. Ardavan, A. M. Bowen, A. Fernandez, A. J. Fielding, D. Kaminski, F. Moro, C. A. Muryn, M. D. Wise, A. Ruggi, E. J. L. McInnes, K. Severin, G. A. Timco, C. R. Timmel, F. Tuna, G. F. S. Whitehead and R. E. P. Winpenny, *npj Quantum Inf.*, 2015, **1**, 1–7.
40 A. Fernandez, J. Ferrando-Soria, E. M. Pineda, F. Tuna, I. J. Vitorica-Yrezabal, C. Knappke, J. Ujma, C. A. Muryn, G. A. Timco, P. E. Barran, A. Ardavan and R. E. P. Winpenny, *Nat. Commun.*, 2016, **7**, 1–6.
41 T. N. Nguyen, W. Wernsdorfer, M. Shiddiq, K. A. Abboud, S. Hill and G. Christou, *Chem. Sci.*, 2016, **7**, 1156–1173.
42 R. Chakrabarty, P. S. Mukherjee and P. J. Stang, *Chem. Rev.*, 2011, **111**, 6810–6918.
43 T. N. Nguyen, M. Shiddiq, T. Ghosh, K. A. Abboud, S. Hill and G. Christou, *J. Am. Chem. Soc.*, 2015, **137**, 7160–7168.
44 W. Wernsdorfer, *Adv. Chem. Phys.*, 2001, **118**, 99.
45 P. M. Lahti and A. S. Ichimura, *J. Org. Chem.*, 1991, **56**, 3030–3042.
46 M. Mitani, H. Mori, Y. Takano, D. Yamaki, Y. Yoshioka and K. Yamaguchi, *J. Chem. Phys.*, 2000, **113**, 4035–4051.
47 J. B. Vincent, H. R. Chang, K. Folting, J. C. Huffman, G. Christou and D. N. Hendrickson, *J. Am. Chem. Soc.*, 1987, **109**, 5703–5711.
48 D. L. Reger, J. R. Gardinier, M. D. Smith and P. J. Pellechia, *Inorg. Chem.*, 2003, **42**, 482–491.
49 See Electronic Supplementary Information (ESI).
50 *SHELXTL2014*, Bruker-AXS, Madison, Wisconsin, USA, 2014.
51 P. Van Der Sluis and A. L. Spek, *Acta Crystallogr.*, 1990, **A46**, 194–201.
52 A. L. Spek, *Acta Crystallogr.*, 2015, **C71**, 9–18.
53 G. A. Bain and J. F. Berry, *J. Chem. Educ.*, 2008, **85**, 532.
54 (*a*) E. R. Davidson, *MAGNET*, Indiana University, Bloomington, IN, 1999; (*b*) E. R. Davidson, *GRID*, Indiana University, Bloomington, IN, 2000.
55 A. K. Hassan, L. A. Pardi, J. Krzystek, A. Sienkiewicz, P. Goy, M. Rohrer and L.-C. Brunel, *J. Magn. Reson.*, 2000, **142**, 300–312.
56 S. Stoll and A. Schweiger, *J. Magn. Reson.*, 2006, **178**, 42–55.
57 T. C. Stamatatos, D. Foguet-Albiol, S.-C. Lee, C. C. Stoumpos, C. P. Raptopoulou, A. Terzis, W. Wernsdorfer, S. O. Hill, S. P. Perlepes and G. Christou, *J. Am. Chem. Soc.*, 2007, **129**, 9484–9499.
58 I. D. Brown and D. Altermatt, *Acta Crystallogr.*, 1985, **B41**, 244–247.
59 G. G. Shan, H.-B. Li, D.-X. Zhu, Z.-M. Su and Y. Liao, *J. Mater. Chem.*, 2012, **22**, 12736–12744.
60 C. Horn, M. Scudder and I. Dance, *CrystEngComm*, 2000, **2**, 196–200.
61 A. M. Mowson, T. N. Nguyen, K. A. Abboud and G. Christou, *Inorg. Chem.*, 2013, **52**, 12320–12322.
62 O. A. Adebayo, K. A. Abboud and G. Christou, *Inorg. Chem.*, 2017, **56**, 11352–11364.
63 T. C. Stamatatos, D. Foguet-albiol, C. C. Stoumpos, C. P. Raptopoulou, A. Terzis, W. Wernsdorfer, S. P. Perlepes and G. Christou, *Polyhedron*, 2007, **26**, 2165–2168.
64 J. H. Van Vleck, *The Theory of Electric and Magnetic Susceptibilities*, Oxford University Press, 1932.
65 R. Tiron, W. Wernsdorfer, D. Foguet-Albiol, N. Aliaga-Alcalde and G. Christou, *Phys. Rev. Lett.*, 2003, **91**, 227203.
66 (*a*) L. Landau, *Phys. Z. Sowjetunion*, 1932, **2**, 46–51; (*b*) C. Zener, *Proc. R. Soc. London, Ser. A*, 1932, **137**, 696–702.
67 R. Tiron, W. Wernsdorfer, N. Aliaga-Alcalde and G. Christou, *Phys. Rev. B: Condens. Matter Mater. Phys.*, 2003, **68**, 140407.
68 R. Bagai, W. Wernsdorfer, K. A. Abboud and G. Christou, *J. Am. Chem. Soc.*, 2007, **129**, 12918–12919.
69 J. Marbey, P. R. Gan, E. C. Yang and S. Hill, *Phys. Rev. B*, 2018, **98**, 144433.
70 S. Hill, S. Datta, J. Liu, R. Inglis, C. J. Milios, P. L. Feng, J. J. Henderson, E. del Barco, E. K. Brechin and D. N. Hendrickson, *Dalton Trans.*, 2010, **39**, 4693–4707.
71 A. Wilson, J. Lawrence, E.-C. Yang, M. Nakano, D. N. Hendrickson and S. Hill, *Phys. Rev. B: Condens. Matter Mater. Phys.*, 2006, **74**, 140403(R).